Title

Sensitivity of subtropical stationary circulations to global warming in climate models: a baroclinic Rossby gyre theory

Journal

Climate Dynamics, 52(7-8)

ISSN

0930-7575

Authors

Levine, Xavier J
Boos, William R

Publication Date

2019-04-01

DOI

10.1007/s00382-018-4419-5

Peer reviewed

Sensitivity of subtropical stationary circulations to global warming in climate models: a baroclinic Rossby gyre theory

Xavier J. Levine[1], William R. Boos[2,3]

1 Barcelona Supercomputing Center, Barcelona, Spain

2 Department of Earth and Planetary Science, University of California, Berkeley, Berkeley, CA, USA

3 Climate and Ecosystem Sciences Division, Lawrence Berkeley National Laboratory, Berkeley, CA, USA

Abstract

Time-mean, zonally asymmetric circulations maintain an intense hydrologic contrast between monsoon regions and subtropical drylands in Earth's present climate. Climate model simulations suggest that this hydrologic contrast will increase in twenty-first-century global warming scenarios, but the response of the zonally asymmetric circulations to global mean temperature is poorly understood. Here we adapt a simple theory for the strength of time-mean, subtropical, zonally asymmetric circulations (hereafter called stationary circulations) and demonstrate its relevance to summer stationary circulation changes in the Northern Hemisphere in an ensemble of comprehensive climate model simulations of global warming. The theory, which is based on the dynamics of a subtropical Rossby gyre that is in Sverdrup balance and has the vertical structure of a first-baroclinic mode, shows that the weakening of stationary ascent with global warming in the multi-model mean can be represented as a compensation between two processes: a lifting of the tropical tropopause and a decrease of the tropospheric zonal temperature gradient, which respectively require strengthening and weakening of vertical mass flux in the Rossby gyre. A large fraction of the intermodel variance in global warming-induced changes in stationary ascent is associated with intermodel variance in zonal tropospheric temperature gradient changes, which we in turn attribute to intermodel variance in zonal sea surface temperature gradient changes. These results show that much of the sensitivity of subtropical hydrologic contrasts to global mean temperature can be understood in terms of a linear vorticity balance and properties of moist adiabats.

Keywords Stationary circulation,· Rossby gyre,· First-baroclinic mode dynamics,·Climate change, CMIP5 archive

1 Introduction

During boreal summer, large zonal asymmetries in tropospheric circulation and hydrology exist in the subtropical Northern Hemisphere. These zonal asymmetries are associated with various diabatic heat sources, in particular the latent heat release of monsoon rainfall and enhanced radiative cooling over subtropical deserts and other regions of time-mean tropospheric subsidence (Webster 1972; Ting 1994; Wang and Ting 1999; Rodwell and

Hoskins 2001; Chen et al. 2001; Yang et al. 2003; Liu et al. 2004). Such planetary-scale circulations are dominant features of summer climate and provide a pathway for changes in one region to remotely affect other regions, e.g. Asian monsoon precipitation driving arid conditions in North Africa and Arabia (Rodwell and Hoskins 1996; Tyrlis et al. 2013; Cherchi et al. 2014).

There is little agreement on how time-mean, zonally asymmetric circulations (hereafter referred to as stationary circulations) may change as climate warms. For instance, while South Asian monsoon winds are expected to weaken in the twenty-first century as greenhouse gas (GHG) concentrations increase (Ueda et al. 2006; Sun et al. 2010; Cherchi et al. 2011), the East Asian monsoon (Sun and Ding 2011; Li et al. 2015) is projected to strengthen. Comprehensive climate models predict a weakening of tropical circulations with global warming, although there is little quantitative agreement on the magnitude of this weakening (Tanaka et al. 2004; Vecchi and Soden 2007). Features such as the Pacific subtropical anticyclone have been predicted to strengthen (Li et al. 2012) or weaken (Shaw and Voigt 2015) depending on which models or strength metrics are used.

This weakening of tropical circulations is qualitatively consistent with a reduction in convective mass flux predicted to occur in the global mean as climate warms (Knutson and Manabe 1995; Held and Soden 2006; Schneider et al. 2010; O'Gorman et al. 2012), but such global mean constraints may not have direct relevance to the future behavior of regional circulations. In general, substantial regional variability of observed trends and large intermodel differences in projected regional trends limit our ability to make robust predictions of regional climate change. Here we aim to provide a more fundamental understanding of the influence of global warming on subtropical stationary circulations in the Northern Hemisphere during boreal summer.

A number of thermodynamic mechanisms have been proposed to explain changes in tropical circulation with global warming. In particular, an increase in static stability—both dry and moist stability—has been suggested as the primary cause of the weakening of tropical circulations (Knutson and Manabe 1995; Chou and Neelin 2004; Ma et al. 2012; He et al. 2017; Wills et al. 2017). Dry static stability is expected to increase as the tropical troposphere shifts to a warmer moist adiabatic temperature profile, while the tropical-mean gross moist stability has been argued to increase as climate warms because of an upward shift in the tropical tropopause and the height of moist convection (Chou and Chen 2010; Chou et al. 2013). However, regional circulation constraints based on such thermodynamic stability arguments are severely limited by possible changes in unconstrained parameters. For instance, an increase in the dry static stability could produce effects smaller than those of changes in the magnitude or spatial structure of precipitation (Muller and O'Gorman 2011). Changes in the diabatic heating of precipitation are indeed an important term in analyses of simulated trends

based on dry static stability constraints (e.g. He et al. 2017). Similarly, an increase in the gross moist stability due to tropopause lifting could be less important for regional climate than changes in sources of moist static energy (e.g. radiative cooling).

Various boundary conditions and radiative forcings have also been shown to influence regional changes in low-latitude circulations with global warming. Sea surface temperature (SST) has been recognized as an important factor in regional climate change, with a global increase in SST promoting ascent over oceans but reducing precipitating ascent over land (Ma et al. 2012; He et al. 2014). Changes in SST gradients also affect the sensitivity of regional circulations and rainfall to global warming. For instance, changes in the spatial pattern of SST over the equatorial Indian and Pacific oceans are associated with changes in the Hadley and Walker circulations in global warming simulations (Xie et al. 2010; Ma and Xie 2013) and in the recent past (Tokinaga et al. 2012). Regional circulations are also influenced by the direct radiative forcing of CO2CO2 (i.e. horizontal gradients in the anomalous tropospheric radiative cooling associated with an increase in greenhouse gas concentration, see Yang et al. 2003; Bony et al. 2013). This direct radiative forcing favors ascent over land but weakens convection over the ocean, strengthening stationary circulations. Accordingly, precipitation may decrease over subtropical oceans but increase over land as climate warms (He and Soden 2017).

Recently, Shaw and Voigt (2015) proposed a simple mechanism to explain this competition between warmer SST and direct CO_2 forcing by considering their respective influence on the moist static energy (MSE) of the subcloud layer: warmer SST increases subcloud MSE over the ocean and direct CO_2 radiative forcing increases subcloud MSE over land. Together, these factors change the contrast in subcloud MSE between land and oceans (Shaw and Voigt 2016a). Given that changes in tropical circulation are tied to near-surface MSE by convection, changes in the land-ocean contrast in subcloud MSE with global warming may influence changes in stationary circulations (Shaw and Voigt 2015) and monsoon strength (Li and Ting 2017). Shaw and Voigt (2015) furthermore showed that this “tug of war” operated in equilibrated simulations of global warming, explaining, for example, the small change of the North Pacific subtropical high.

Although recent progress has thus been made, a theory that quantifies the influence of boundary conditions and forcings on stationary circulations is still outstanding. Here we take a dynamical approach to understanding changes in subtropical circulations by focusing on the building block of zonal asymmetries in subtropical climate: the stationary Rossby wave. As mentioned above, stationary Rossby waves couple precipitation in monsoon regions such as South Asia and North America with expansive dry regions to the west (Rodwell and Hoskins 1996, 2001). These Rossby waves are baroclinic, with lower- and upper-tropospheric horizontal winds having opposite signs; precipitating ascent occurs in regions of poleward flow and

subsidence occurs in regions of equatorward flow in a state of Sverdrup balance. We recently proposed a mechanism (Levine and Boos 2016) based on the first-baroclinic mode, Sverdrup-balanced dynamics of a subtropical Rossby gyre to explain why the strength of subtropical stationary circulations scaled non-monotonically with global mean temperature in an aquaplanet idealization of Earth's subtropics. Convective quasi-equilibrium and Sverdrup balance—the fundamental assumptions of our mechanism—are characteristics of large-scale tropical circulations that have been used in past studies to understand changes in tropical circulation in present-day climate and with climate change (Chen 2010; Shaw and Voigt 2016b). These assumptions were combined to devise an analytical prediction for the sensitivity of stationary Rossby waves to climate change (Levine and Boos 2016). In our mechanism, the weakening of stationary ascent was attributed to changes in two boundary conditions. First, the tropopause lifting that occurs with global warming causes a strengthening of large-scale zonally asymmetric vertical motions in a state of Sverdrup balance, given a fixed zonal temperature gradient. Second, the ocean surface energy budget requires a weakening of zonal sea surface temperature gradients with global warming (Knutson and Manabe 1995; Merlis and Schneider 2011), thereby weakening large-scale zonally asymmetric vertical motions. Quantitatively, the tropopause lifting dominates in cold climates, while the weakening of zonal SST gradients dominates in warm climates, producing a non-monotonic dependence on global mean temperature of zonal asymmetries in ascent, at least in our aquaplanet simulations (Levine and Boos 2016).

Here we examine whether this mechanism holds in an ensemble of comprehensive climate models with realistic boundary conditions and forcings. We assess the ability of this mechanism to explain the multi-model mean weakening of simulated stationary circulations with global warming in the Northern Hemisphere subtropics in summer, and its ability to account for intermodel variability in changes in simulated subtropical climate with global warming.

2 Data and metrics

We compare boreal summer (June–September) climatologies simulated by 39 models of the Coupled Model Intercomparison Project Phase 5 (CMIP5; see Table 1 for a list of GCMs and variables). Model output was downloaded and diagnostics were computed on the native grid before being re-gridded on a 1◦×1 horizontal grid. For each model as well as for the ensemble-mean of all models, we compare changes between simulated boreal summer climates of recent historical times (1985–2004) and the end of the twenty-first century (2076–2095) under Representative Concentration Pathway (RCP) 8.5, a "business-as-usual" emission scenario (Taylor et al. 2012). Changes between these two time periods are normalized by near-surface temperature change horizontally averaged over a subtropical domain (10◦N to 40◦N), and may also be expressed as relative changes (in percent),

$$\Delta(.) = \frac{(.)|_{\mathrm{RCP8.5}} - (.)|_{\mathrm{HIST}}}{T_{2m}|_{\mathrm{RCP8.5}} - T_{2m}|_{\mathrm{HIST}}}, \quad (1)$$

$$\delta(.) = \Delta(.) \times \frac{100}{(.)|_{\mathrm{HIST}}}. \quad (2)$$

Here T_{2m} is the air temperature 2 meters above the surface averaged over 10°N to 40°N. The CMIP5 historical climatology is also compared to the climatology for the same years (1985–2004) from the ERA-Interim reanalysis (Dee et al. 2011).

Here we focus on stationary circulations in the Northern Hemisphere (NH) subtropics, with the stationary component of any quantity defined as the zonally asymmetric part of the time-mean of that quantity. We define the NH subtropics as the 10°N to 40°N latitudinal band, which contains nearly all subtropical deserts in the Northern Hemisphere, as well as nearly all of the East and South Asian monsoon regions. To provide a scalar metric of the amplitude of the stationary component, we define a spatial integral over the NH subtropics,

$$\langle X \rangle(p) = \int_{\mathscr{A}} -X(\mathbf{x}, p)\mathscr{H}(-X(\mathbf{x}, p))\,\mathrm{d}A, \quad (3)$$

where A is horizontal area, $\mathscr{A}$ is the domain of integration, i.e. the 10°N to 40°N latitudinal band, and $\mathscr{H}$ is the Heaviside function. This spatial integral (over all locations **x** in the horizontal plane) defines bulk values, ⟨X⟩, for every pressure level p. We will focus on the vertical mass flux in the stationary circulation by applying this metric to the stationary vertical wind, $\langle \omega * \rangle$, with ω the vertical velocity and $(.)*$ the deviation from the zonal mean. Other metrics have been used to quantify stationary anomalies on a global scale, such as the root mean square of the stationary eddy vertical wind (e.g. Shaw and Voigt 2016b). The bulk metric $\langle \omega * \rangle$ is chosen instead as it provides a direct measure of the time-mean vertical mass flux in stationary circulations, rather than a measure of the spatial variance of vertical velocity. Note that without the Heaviside function $\mathscr{H}$, $\langle \omega * \rangle$ would be identically zero as zonal asymmetries vanish in the zonal mean.

3 Results

3.1 Response to global warming simulated by climate models

Subtropical climate is characterized by large zonal asymmetries in tropospheric circulation and hydrology during boreal summer. This is clearly shown by vertical wind in the historical simulations: when evaluated at 400 hPa, a succession of ascent and descent zones in the NH subtropics are

found in the ensemble-mean (Fig. 1a), consistent with continental deserts, oceanic highs, and monsoon regions being found in that same latitudinal band.

A longitudinal profile of the 400 hPa stationary vertical wind averaged over the NH subtropics clearly shows extensive regions of ascent over South Asia, the eastern Indian and western Pacific oceans, and Central and North America (Fig. 1c; note that ascent is defined by negative values). Conversely, broad regions of descent are found over the Mediterranean, the eastern Atlantic, and the eastern Pacific oceans. These zonal asymmetries dominate regional climate over most of the tropics, especially north of about 20°N where the zonal-mean summer Hadley cell strength is weak (Fig. 1b). Nevertheless, zonal-mean ascent or descent can be comparable to stationary vertical wind in some regions, especially in the deep tropics (equatorward of 20°N) and in the SH tropics (40°S to 0°N), where the winter cross-equatorial Hadley cell is considerably stronger than the summer Hadley cell (Fig. 1b).

As climate warms, stationary and zonal-mean vertical wind changes are generally of opposite sign to that of the present-day climatology, suggesting a general weakening of the subtropical circulation (Fig. 1d, e). This is qualitatively consistent with previous studies of comprehensive and idealized climate models (Vecchi and Soden 2007; Seager et al. 2010). However, the weakening is not spatially uniform, with large subtropical dynamical changes in the NH subtropics found over the western Atlantic, the eastern Mediterranean, and East Asia (Fig. 1d), consistent with large regional differences in the sensitivity of vertical mass flux and precipitation to climate change (Seager et al. 2010; Scheff and Frierson 2012). In contrast, circulation changes in the western Pacific appear to be small, in agreement with the findings of Shaw and Voigt (2015). The apparent westward shift of the Atlantic and Pacific subtropical anticyclones is a robust feature of simulations of global warming (Shaw and Voigt 2015), and has been attributed to changes in patterns of convective heating over oceans (Zhou et al. 2009), land-sea thermal contrast (Li et al. 2012), and increased radiative forcing over land (Shaw and Voigt 2016a; Kelly et al. 2018).

3.2 Describing a moist, first-baroclinic stationary Rossby gyre

Earth’s subtropical stationary circulations can be reproduced by prescribing diabatic heat sources and zonal-mean flow in dry models, with the essential response described by linear dynamics (Rodwell and Hoskins 1996). When forced by a subtropical heat source, the atmosphere responds by generating stationary Rossby waves whose spatial structures can be described analytically (Gill 1980). Such models demonstrate the relevance of the time-mean Rossby wave associated with monsoon rainfall (Wang and Ting 1999; Rodwell and Hoskins 2001; Chen et al. 2001; Liu et al. 2004); during summer, diabatic heating associated with monsoon rainfall occurs in the

zonally narrow, ascending branch of the Rossby wave while descent occurs in the zonally broad region to the west.

Here we posit that some of the basic dynamical balances inherent in these stationary, baroclinic Rossby waves can aid in understanding the response of subtropical climate to global warming. In particular, we use the fact that subtropical circulations are approximately in Sverdrup balance (Chen et al. 2001; Liu et al. 2004), and that low-latitude Rossby waves have a first-baroclinic mode structure with vertical winds being maximum in the mid-troposphere (around 500 hPa). This baroclinic structure is a robust feature of Earth's summer circulations (Trenberth et al. 2000), as expected for horizontally divergent circulations in a moist-convecting atmosphere (Neelin 2007). Since our approach will be based on a linear Sverdrup balance, it differs from the nonlinear limit discussed by Emanuel (1995), who also used a convective quasi-equilibrium system to solve for the vertical velocity, but assumed ascent would occur when the upper troposphere reached the nonlinear, zero absolute vorticity limit. Our treatment is similar to a linearized form of the Emanuel (1995) theory, but with the addition of Sverdrup balance to obtain the full horizontal distribution of vertical motion.

In previous work, we devised separate scalings for the vertical mass flux that can be obtained from Sverdrup balance and for the vertical mass flux arising from Ekman convergence in the planetary boundary layer (Levine and Boos 2016). Here we examine only the first, inviscid scaling and its applicability to the CMIP5 models. In summary, we first isolate the component of vertical wind associated with baroclinic flow (e.g. that in a baroclinic Rossby wave),

$$\omega_g = \frac{\beta}{f}\int_{p_s}^{p} v_g \, \mathrm{d}p, \tag{4}$$

where

$$v_g(p) = \frac{R_d}{f}\left(\int_{p_s}^{p} \partial_x T \, \mathrm{d}\log p - \frac{1}{p_t - p_s}\int_{p_s}^{p_t}\int_{p_s}^{p} \partial_x T \, \mathrm{d}\log p \, \mathrm{d}p\right). \tag{5}$$

Here, (5) specifies the meridional wind v_g that is in geostrophic balance with the zonal temperature gradient, $\partial_x T$, having removed the barotropic component of the geostrophic wind (via the double integral in the last term). This vertical integral is confined to the troposphere, i.e. between surface pressure p_s and tropopause level p_t; R_d is the gas constant of dry air and f the Coriolis parameter. The vertical wind that is in Sverdrup balance with this baroclinic component of the meridional wind is given by ω_g in (4). By definition, ω_g integrates to zero in the zonal mean for isobars not intersecting the surface, and so projects entirely on the stationary vertical wind; the actual zonal mean of ω_g will not be exactly zero because isobars do intersect the surface, in particular near mountain ranges. The balances (4) and (5) can

be applied everywhere except near the equator where the Coriolis parameter f vanishes; this is not an issue here since we focus on regions poleward of 10°N.

In the present-day climate (1985–2004) the Sverdrup-balanced, baroclinic vertical wind, ω_g, shows a broad region of ascent in the western Pacific and a smaller region of ascent centered in the Caribbean; large-scale descent is found over much of Arabia, North Africa, the eastern Atlantic, and off the coast of California (Fig. 2a). In Sverdrup balance, ascent is associated with lower-tropospheric poleward wind in the Northern Hemisphere. Over Southeast Asia for instance, ascent is associated with the low-level poleward monsoon flow, while descent over the eastern Mediterranean regions occurs in low-level equatorward flow (the Etesian winds). There are substantial differences between ω_g and ω^*, In particular over land where ω_g is generally weaker than ω^*; this is consistent with the existence of other components of ω^*, such as boundary layer Ekman flow (e.g. Wills and Schneider 2015; Shaw and Voigt 2016b). Over land, the dynamical balance can be especially complex near mountain ranges (which introduce mechanical lifting). Here we do not consider those ageostrophic components of the flow, in part because ω_g seems to capture much of the spatial variability in ω^* over oceans, despite a substantial zonal and meridional shift between extrema in ω_g and ω^*. Because of this zonal and meridional offset in their spatial structures, the horizontal distributions of ω^* and ω_g are found to be only modestly correlated locally (R=0.48). Nevertheless, the zonal correlation between ω^* and ω_g is largest in the NH subtropics (see cyan line in Fig. 3a), in agreement with Sverdrup balance being the dominant dynamical balance there. Furthermore, when averaged over the NH subtropics (10°N–40°N), zonal profiles of ω^* and ω_g show a similar succession of ascent and descent zones (Fig. 2c) which are well correlated (R=0.66).

Changes in ω_g with global warming show spatial similarities with changes in ω^*, generally indicating a weakening and westward shift of the pattern of vertical motion (Fig. 2d), consistent with the westward shift of subtropical anticyclones seen in simulations of global warming (e.g. Shaw and Voigt 2015, 2016a; Kelly et al. 2018). Because the spatial pattern of these changes is shifted, the spatial correlation between $\blacktriangle\omega^*$ and $\blacktriangle\omega_g$ is weak (R=0.38). But changes in ω_g and ω^* are better correlated at northern subtropical latitudes (i.e., between 10°N–40°N) than in any other region (Fig. 3d). When averaged over the NH subtropics, changes in ω_g and ω^* have a spatial correlation coefficient of near 0.7 (Fig. 2f), which also supports the hypothesis that a large part of the changes in ω^* can be understood through constraints on ω_g.

We now use our metric for the spatially integrated strength of a stationary anomaly, defined in (3), to assess the vertical structure of stationary ascent and its Sverdrup-balanced, baroclinic component in the NH subtropics. The integrated stationary ascent, $\langle\omega^*\rangle$, peaks near 700 hPa in both the historical and RCP8.5 simulations (Fig. 4a) and is roughly constant between 700 and

400 hPa. The ensemble-mean simulated $\langle \omega^* \rangle$ has a much weaker lower-tropospheric peak than ERA-Interim, possibly indicating that the CMIP5 models have strong bias in the Ekman or boundary-layer component of ascent associated with shallow convection and surface drag. There is closer agreement between the CMIP5 ensemble-mean and ERA-Interim above 600 hPa. Mass flux in the stationary component of ascent peaks near 1500 Sv (with 1 Sv = 10^9 kg/s), which is more than an order of magnitude larger than the annual-mean NH Hadley cell mass flux of about 92 Sv (averaged between 1980 and 2001 in ERA-40). The spatially integrated Sverdrup-balanced baroclinic ascent, $\langle \omega_g \rangle$, peaks at 500 hPa and has an ensemble-mean strength near 1100 Sv (Fig. 4b). While the vertical structures of $\langle \omega^* \rangle$ and $\langle \omega_g \rangle$ are similar above 600 hPa, there are substantial differences in the lower troposphere—particularly for ERA-Interim—that suggest ageostrophic flow may be important there.

In summary, the Sverdrup-balanced baroclinic vertical wind accounts for roughly half the spatial variance in stationary ascent and its change in a global warming scenario in the NH subtropics. In particular, stationary vertical wind and its Sverdrup-balanced, baroclinic component both weaken in the troposphere, except in the upper troposphere where both quantities strengthen (Fig. 4a, b). In the next section, we explain the magnitude and vertical structure of these changes using a simple dynamical theory.

3.3 A simple dynamical theory for stationary circulation strength

Motivated by the similarities between $\langle \omega^* \rangle$ and $\langle \omega_g \rangle$ presented above, we describe changes in stationary circulations with climate change using a Sverdrup-balanced state in a first-baroclinic mode framework. This framework considers the vertical structure of the stationary circulation to be set by the fundamental moist convective properties of the troposphere, independent of circulation itself (Yu et al. 1998). In short, the vertical structure of winds is set by the moist adiabatic structure of temperature variations, assuming that moist convection is sufficiently active to keep the temperature structure of the low-latitude troposphere near that of a moist adiabat (Neelin and Zeng 2000).

As mentioned in Sect. 1, Levine and Boos (2016) combined such a first-baroclinic mode framework with a linear vorticity balance, devising a simple analytical model for stationary circulation variability. That model captured stationary circulation changes simulated in a moist aquaplanet GCM over a wide range of climates and attributed those changes to changes in zonal SST gradient and tropopause level. Here we use a similar approach, motivated by the fact that the Rossby waves dominating the summer climate of the NH subtropics are nearly in Sverdrup balance (Chen et al. 2001; Liu et al. 2004). We do not address other contributions to changes in vertical winds, e.g. Ekman ascent or orographic lifting. Despite the simplicity of this treatment, the correspondence between stationary vertical wind and its Sverdrup-balanced baroclinic component in the NH subtropics (Figs. 2, 4) suggests it

may provide insight on the spatial variability of summer stationary circulations.

3.3.1 Assessing the first-baroclinic mode structure of temperature variations

Atmospheric first-baroclinic mode dynamics relies on tropospheric temperature adjusting quickly to thermodynamic anomalies in the subcloud layer, at least in convecting regions (Neelin and Yu 1994). Yet tropospheric temperature can be decoupled from the subcloud layer over large swathes of the tropics, for instance in regions of large-scale subsidence (Brown and Bretherton 1995). Here we assume that moist static energy (MSE) anomalies in the subcloud layer translate into temperature anomalies in the free troposphere on large scales; specifically, spatially integrated anomalies in subcloud MSE are assumed to equal spatially integrated anomalies in saturation MSE above the lifting condensation level (LCL),

$$\langle h^{sat*} \rangle(p) = \langle h_b^* \rangle \simeq \langle h_s^* \rangle, \qquad (6)$$

where h_b is subcloud MSE and h_s the near-surface (2-m) value of MSE (the 2-m value of MSE is assumed to be representative of its average subcloud value). Using (6), temperature anomalies in the free troposphere can be expressed in terms of those evaluated at a reference level (above the LCL),

$$\langle T^* \rangle(p) = \langle T_1^* \rangle A_1(p). \qquad (7)$$

Here T_1 is a temperature anomaly, at reference level p_1, with respect to a reference temperature profile T_0, i.e. $T(\mathbf{x}, p) = T_0(p) + T_1(\mathbf{x}) A_1(p)$. In (7), which holds only above the subcloud layer, the temperature mode A1A1 defines the sensitivity of tropospheric temperature to temperature anomalies at the reference level; its profile can be derived directly from the convective quasi-equilibrium condition (6). The temperature mode depends on variables that vary only weakly in space in the tropics, i.e. lapse rate and tropopause level (see “Appendix”), so A_1 is set to depend only on vertical level in (7). Both (6) and (7) state that tropospheric temperature anomalies can be related to subcloud MSE anomalies and thus, if near-surface relative humidity is nearly invariant as it is over oceans, to near-surface temperature (see Schneider et al. 2010). On large scales, (7) predicts that tropospheric temperature (or saturation MSE) anomalies above the subcloud layer will be coherent vertically and covary with subcloud MSE (and with near-surface temperature over oceans).

To assess the relevance of (6) and (7) to simulations of climate change, we compare changes with global warming in the stationary components of near-surface MSE and tropospheric saturation MSE, spatially integrated over the NH subtropics (Fig. 5). When evaluated at 400 hPa, there is substantial inter-model scatter in the relationship between $\langle h^{sat*} \rangle$ and $\langle h^*_s \rangle$, but the best linear fit of the relationship lies nearly on the one-to-one line and the two have a correlation coefficient of nearly 0.8 (Fig. 5a). This indicates that much inter-

model variability can be explained by the convective quasi-equilibrium relation (6). Furthermore, the multi-model mean changes in $\langle h^{sat*} \rangle$ and $\langle h^*_s \rangle$ are also nearly equal, lying on the one-to-one line at values near 4%/K. The association between $\langle h^{sat*} \rangle$ and $\langle h^*_s \rangle$ holds through the depth of the upper troposphere, as shown by regression and correlation coefficients being nearly invariant between 500 and 200 hPa (Fig. 5b, c). Relation (6) fails in the lower troposphere, i.e. below 500 hPa, where saturation MSE anomalies depart significantly from anomalies in near-surface MSE. These deviations from convective quasi-equilibrium may result from shallow convection (moist or dry) strongly influencing the thermal stratification of the lower troposphere in comprehensive climate models. Despite this limitation, changes in saturation MSE in the upper troposphere are broadly consistent with those predicted from near-surface MSE anomalies using (6).

3.3.2 Defining the first-baroclinic mode of balanced, stationary ascent

We now use the moist adiabatic temperature structures (7) together with our definition of the Sverdrup-balanced vertical wind (4) to define the first-baroclinic component of the Sverdrup-balanced vertical wind. To begin, we assume the horizontal and vertical structures of the stationary temperature anomalies are separable,

$$T^*(\mathbf{x}, p) = \langle T^* \rangle (p) \Gamma(\mathbf{x}), \tag{8}$$

with Γ being a normalized horizontal structure function, i.e. $\langle \Gamma \rangle = 1$, that is invariant with height. Combining (7) and (8), tropospheric temperature anomalies above the subcloud layer are expressed as

$$T^*(\mathbf{x}, p) = \langle T_1^* \rangle A_1(p) \Gamma(\mathbf{x}). \tag{9}$$

As mentioned in the previous subsection, T_1 defines a temperature anomaly, with respect to the tropical mean, at a particular reference level p_1. Here we set p_1 to 400 hPa, choosing an upper-tropospheric level to be consistent with the idea that temperature anomalies are more directly controlled by deep convection in the upper than in the lower troposphere (as suggested by Fig. 5b, c).

Combining (4), (5), and (9), we obtain an expression for stationary vertical wind in the NH subtropics,

$$\omega_{g1}(\mathbf{x}, p) = R_d \frac{\beta}{f^2} \langle T_1^* \rangle \partial_x \Gamma(\mathbf{x}) \, \Omega_1(p), \tag{10}$$

This relation is nearly identical to that derived in Levine and Boos (2016), except that the horizontally integrated temperature gradient has been decomposed into an amplitude, $\langle T^*_1 \rangle$, and a horizontal structure function Γ. Although (10) might at first glance seem to depend only on the horizontal distribution of temperature via $\langle T^*_1 \rangle \langle \, \rangle$ and Γ, the vertical wind mode, Ω_1,

depends on both the temperature mode, A_1, and the tropopause level, p_t (for details see “Appendix”). In practice, changes in Ω_1 with global warming are found to be mostly associated with changes in tropopause level (see Sect. 3.5.1; Levine and Boos 2016).

3.4 Predicting subtropical climate change from the simple theory

We will now use (10) to quantitatively relate variations in subtropical stationary circulations and in zonal hydrologic asymmetries to variations in tropospheric temperature. For a global warming scenario, we will consider both the CMIP5 multi-model mean changes and variations within the model ensemble. We go beyond the simple diagnosis of the Sverdrup-balanced wind that was performed in Sect. 3.2, using the first-baroclinic mode theory outlined above to predict changes in ascent from changes in near-surface MSE and SST.

3.4.1 Stationary circulation changes

The first-baroclinic vertical wind $\omega_g 1$ defined in (10) is found to be broadly consistent with the Sverdrup-balanced, baroclinic vertical wind ω_g, and with the total stationary vertical wind ω^*. When evaluated at 400 hPa, the spatial patterns of $\omega_g 1$ and $\Delta\omega_{g1}$ are found to be highly similar to those of ω_g and $\Delta\omega_g$ (compare Fig. 2a, d with Fig. 3a, c). Zonal variations in $\omega_g 1$ are most strongly correlated with ω^* in the NH subtropics (red line in Fig. 3b), in qualitative agreement with the strong zonal covariance of ω_g with ω^* (cyan line in Fig. 3b). When meridionally averaged over the NH subtropics, $\omega_g 1$ and ω_g vary similarly with longitude at 400 hPa (Fig. 2c), as do their changes with global warming (Fig. 2f). Furthermore, changes in meridionally averaged first-baroclinic vertical wind correlate well with changes in stationary vertical wind, with a correlation coefficient exceeding 0.7 in the NH subtropics (Fig. 2f). The comparison shown in Fig. 2f constitutes a test of the predictions made by (10), and could have revealed the importance of processes not accounted for in our theory, such as boundary-layer Ekman flow, deviations from the first-baroclinic mode, or lack of vertical coherence of temperature anomalies in the tropical troposphere. The decent match between the red and black lines instead supports the idea that Sverdrup balance, convective quasi-equilibrium, and first-baroclinic mode dynamics are highly relevant to changes in stationary ascent over large swathes of the NH subtropics during summer.

The ensemble-mean, spatially integrated vertical profile of Sverdrup-balanced, first-baroclinic ascent $\langle\omega_{g1}\rangle$ is nearly identical to that of Sverdrup-baroclinic vertical wind $\langle\omega_g\rangle$ through most of the troposphere (compare Figs. 4b and 6b). First-baroclinic ascent weakens as climate warms over most of the troposphere, consistent with the apparent weakening of stationary ascent and of its Sverdrup-baroclinic component (compare Figs. 4a, b and 6b). A more detailed analysis confirms that changes in these various components of the vertical wind indeed have similar vertical profiles above the 500 hPa level, with the mass flux generally weakening in the troposphere

except in its uppermost levels (i.e. above the 300 hPa level) where it strengthens (Fig. 7a). Differences between the vertical profiles of changes in stationary ascent and first-baroclinic ascent are small in the upper troposphere (i.e. 500–200 hPa), and likely result from contributions to the large-scale circulations that were neglected when devising first-baroclinic wind scaling (10), e.g. Ekman ascent, orographic lifting, and nonlinear contributions. Nonetheless, decent agreement between stationary vertical wind and Sverdrup-balanced, first-baroclinic vertical wind profiles confirms the relevance of our first-baroclinic mode framework and Sverdrup balance to subtropical summer circulations.

3.4.2 Hydrological imbalance changes

We now examine whether changes in the zonally asymmetric component of the hydrological cycle can be understood using our framework for changes in ω_{g1}. By combining our expression for the spatially integrated first-baroclinic vertical wind $\langle\omega_{g1}\rangle$ with a spatially averaged saturation specific humidity profile q_0^{sat}, we devise an expression for the zonally asymmetric part of the surface hydrologic imbalance (i.e. precipitation minus evaporation, $P-E$) in the NH subtropics,

$$\langle P-E\rangle_{g1} = \frac{rh}{g}\int_{p_t}^{p_s}\langle\omega_{g1}\rangle\langle\partial_p q_0^{sat}\rangle\,\mathrm{d}p. \qquad (11)$$

Here, *rh* represents the relative humidity of the tropical atmosphere and is set to 0.8. While relative humidity varies across models and locations, those variations appear to be less important for driving variations in $P-E$ than variations in vertical wind or temperature [the 0.8 value was chosen to optimize the comparison between observed and predicted $\langle(P-E)*\rangle$, but is consistent with commonly used estimates for oceanic boundary layer relative humidity (e.g. Held and Soden 2000)]. Scaling (11) has been found to hold well in the tropics in idealized climate model simulations (Levine and Boos 2016). It is derived from a more accurate approximation of the zonally asymmetric part of the surface hydrologic imbalance that uses vertical wind ω^* instead of ω_{g1}, and which has been found to accurately capture variability in $P-E$ in comprehensive climate models (Seager et al. 2010; Chou and Chen 2010). When deriving scaling (11), contributions from time-mean horizontal advection of moisture and transient eddies are ignored; their contributions to changes in the hydrologic imbalance are indeed small in summer over most subtropical zones in comprehensive model simulations of future climate scenarios (Seager et al. 2014a, b).

The relevance of (11) to simulations of future climate change is assessed by comparing changes in the spatially integrated stationary component of $P-E$, $\langle(P-E)*\rangle$ to its predicted changes with global warming (11) when accounting for both variations in mass flux ω_{g1} and specific humidity q_0^{sat}

(Fig. 7b). The multi-model mean change in $\langle (P-E)* \rangle$ is about 4%/K while the value predicted by (11) is about 6%/K. The prediction based on (11) accounts for about half of the intermodel variance in $\langle (P-E)* \rangle$, although deviation of the best linear fit from the one-to-one line indicates that the simulated change in $\langle (P-E)* \rangle$ is generally overpredicted by (11). From relation (11) we quantify the influence of dynamic and thermodynamic changes on stationary $P-E$: in qualitative agreement with previous studies (Vecchi and Soden 2007), the 6%/K increase in $\langle (P-E)* \rangle_{g1}$ in the multi-model mean results from a partial cancellation of the specific humidity increase (8%/K) by the stationary ascent weakening (− 2%/K; see blue and red stars in Fig. 7b). However, most of the intermodel scatter is dominated by variability in stationary ascent (not shown), in agreement with the sensitivity of specific humidity to global warming being constrained by the Clausius–Clayperon relation and simulated consistently by climate models (Chou et al. 2009).

3.5 Analysis of factors associated with stationary circulation changes

Since the first-baroclinic vertical wind model (10) is a decent proxy for a large part of the stationary circulation changes with global warming (e.g. Figs. 2f, 7a), we now examine the main drivers of changes in the strength of the first-baroclinic stationary ascent. Linearizing changes in spatially integrated first-baroclinic ascent (10) relates changes in the strength of that ascent to changes in the amplitude of temperature anomalies, changes in the horizontal structure of temperature anomalies, and changes in the vertical structure of ascent,

$$\delta\langle\omega^*\rangle(p) \simeq \delta\langle\omega_{g1}\rangle(p) = \delta\langle T_1^*\rangle + \delta\langle\partial_x \Gamma\rangle + \delta\Omega_1(p). \qquad (12)$$

The competition between the weakening of zonal temperature gradients (resulting from changes in the amplitude and horizontal structure of temperature anomalies) and the strengthening of the vertical wind mode results in a weakening of stationary ascent in the middle troposphere (between 700 and 300 hPa), and a strengthening in the uppermost troposphere (above 300 hPa; compare blue, red, and cyan lines in Fig. 7a). We now describe the contribution of each of these components to stationary vertical wind changes in both the ensemble-mean and intermodel variability.

3.5.1 Ensemble-mean changes

Changes in the vertical wind mode Ω_1 describe how warming alters ascent through the influence of changes in the moist adiabatic vertical profile of temperature. In the ensemble-mean, Ω_1 strengthens at all levels, at rates steeply increasing at higher levels (Fig. 6 and cyan line in Fig. 7a). As discussed in Levine and Boos (2016), most of this strengthening is caused by tropopause lifting (see cyan dotted line in Fig. 8a), with only a modest contribution from changes in the temperature mode (cyan dashed line in Fig. 8a): as the tropopause lifts, a fixed horizontal temperature gradient must be accompanied by an increase in the vertically integrated horizontal convergence as the first-baroclinic horizontal wind convergence strengthens

and the layer over which that convergence occurs deepens (Levine and Boos 2016). The strong increase in the rate of change of Ω_1 in the uppermost troposphere results from normalizing changes by the historical climatology, as the climatological vertical wind is weak there.

An opposing effect is associated with horizontal temperature gradients at the reference level weakening as climate warms (blue line in Fig. 7a). This weakening is driven by changes in the horizontal structure function Γ and changes in spatially integrated temperature anomalies $\langle T^*_1 \rangle$, which contribute nearly equally to the weakening in the ensemble-mean (blue dashed and dotted lines in Fig. 8a). This finding is broadly consistent with the weakening of monsoon circulations documented in previous studies over India (Sun et al. 2010; Sun and Ding 2011; Dai et al. 2013; Ma and Yu 2014), but emphasizes changes in zonal rather than meridional temperature gradients.

3.5.2 Intermodel variability

In addition to explaining some of the ensemble-mean changes, our Sverdrup-balanced, first-baroclinic wind framework can account for more than half of the intermodel variance in stationary vertical wind changes with global warming.

In the ensemble-mean, changes in zonal temperature gradients and in the vertical wind mode contribute similarly to changes in stationary ascent (Fig. 7a), but intermodel variability in stationary ascent changes is dominated by temperature gradient changes. In particular, this intermodel variability is dominated by changes in the spatially integrated zonal temperature anomaly $\delta\langle T^*_1 \rangle$ (Fig. 8b). That is, intermodel variations in stationary vertical wind changes with global warming are dominated by changes in the magnitude of temperature deviations from the zonal mean. In comparison, the contribution of changes in the horizontal structure function Γ is small (blue dotted line in Fig. 8b), and that of changes in the vertical wind mode Ω_1 is modest (as seen from the dominant contribution of tropopause level changes shown by the cyan dotted line in Fig. 8b). The modest contribution of the vertical wind mode to intermodel variability in stationary ascent changes is perhaps unsurprising because that mode depends only on the tropopause level and lapse rate averaged over the NH subtropics, which are well constrained by the moist convective lapse rate and tropical-mean sea surface temperature (Reid and Gage 1981) and are thus represented similarly in climate models (especially when normalized by the NH subtropical mean temperature change). The lack of substantial intermodel variability in the horizontal structure function Γ suggests that the spatial pattern of tropospheric temperature change is similar across models (at least after a spatial integral of the rectified zonally asymmetric component is taken), even if the magnitude of the temperature change varies widely across models. In summary, changes in the horizontal structure

of monsoonal lows and oceanic highs are similar across climate models, but changes in their intensity may vary greatly.

The robust association between changes in stationary ascent and temperature anomaly $\langle T^*_1 \rangle$ across models suggests that near-surface MSE may be a useful indicator (or perhaps even a driver) of changes in stationary ascent, because changes in near-surface MSE anomalies translate into changes in deep-tropospheric temperature anomalies, as represented by the quasi-equilibrium relation (6). As shown in Fig. 5a, changes in spatially integrated near-surface MSE anomalies vary widely across models (from about − 2 to 10%/K), and are associated with large intermodel differences in changes in zonal temperature gradients and stationary ascent. In the ensemble-mean of CMIP5 simulations, near-surface MSE and tropospheric saturation MSE anomalies both increase at about 4%/K as climate warms (Fig. 5a); because of the nonlinear dependence of saturation MSE on temperature, this corresponds to a weakening of tropospheric temperature anomalies of about − 1%/K and contributes to the weakening of stationary ascent with global warming (Fig. 8a).

Because near-surface MSE over the oceans is tightly coupled to SST, these results provide a mechanism for SST patterns to affect the sensitivity of stationary ascent to climate change. Although our results cannot rule out the converse mechanism—stationary circulation changes driving SST changes—the idealized GCM results and analysis presented by Levine and Boos (2016) support the hypothesis that SST changes cause the circulation changes. While SST is known to be an important driver of circulation changes in climate models (Xie et al. 2010; Ma and Xie 2013), our mechanism (10) emphasizes the critical role played by its zonal asymmetries in forcing subtropical large-scale ascent.

3.6 Intermodel variability in regional climate change

Now we characterize the horizontal structure of changes in stationary ascent, $P-E$, and other quantities that were described above primarily in terms of horizontally integrated metrics. We define a coupling index,

$$I(\Delta X, \delta\langle\omega^*\rangle_r) = \frac{\partial \Delta X}{\partial \delta\langle\omega^*\rangle_r}\sigma\left(\delta\langle\omega^*\rangle_r\right), \qquad (13)$$

which quantifies local variations in the changes of environmental variable X associated with changes in the horizontally integrated stationary ascent, $\delta\langle\omega^*\rangle_r$. Here, $(.)_r$ denotes a property of the 400 hPa level and $\sigma(.)$ is the intermodel standard deviation.

The similarity between the patterns of basic state ω^* (Fig. 1c) and of this coupling index (Fig. 9a) in the NH subtropics confirms that models with a stronger horizontally integrated stationary ascent exhibit a straightforward amplification of the pattern of multi-model mean stationary ascent. In particular, ascent in the West Pacific and Caribbean and descent in the West

Indian and East Pacific oceans are intensified in simulations in which integrated stationary ascent strengthens more than the ensemble-mean (Fig. 9a). Intermodel variations are largest in the southern part of our subtropical NH band and in equatorial and SH regions outside of that band, i.e. in regions strongly influenced by monsoons over land and the marine ITCZ over oceans. Consistent with this pattern, increases in $P-E$ in the West Pacific and decreases in $P-E$ in the East Pacific are stronger in simulations with stronger integrated stationary ascent (Fig. 9b); this regression also shows that stronger rainfall over South Asia and the West Pacific is associated with an equatorward shift of the ITCZ over the East Pacific and East Atlantic oceans, which suggests that these large regional changes in $P-E$ between land and ocean translate to only modest variations of the zonal-mean ITCZ (not shown).

The coupling index (13) can also be used to characterize the spatial pattern of changes in near-surface MSE and SST associated with changes in spatially integrated stationary ascent. The zonal contrast in near-surface MSE increases in the subtropical NH as stationary ascent strengthens more than the ensemble-mean (Fig. 10a), with positive anomalies over regions that have high MSE in the climatological mean (South Asia, the West Pacific, and the Gulf region of North America) and negative anomalies over regions with low climatological mean MSE (the East Pacific, East Atlantic, and Sahara). Over ocean regions, changes in SST look like the changes in near-surface MSE (Fig. 10b), as is expected from near-surface MSE being well constrained by SST over oceans (Schneider et al. 2010). This similarity in the spatial pattern of near-surface MSE and ocean surface temperature suggests that an increase in the zonal asymmetry of SST in the subtropical NH may be causing the increase in stationary ascent, as quantified by our mechanism (10).

These increases in the zonal contrast of SST and near-surface MSE are associated with an increase in the interhemispheric SST difference (Fig. 10b). In particular, anomalous warming of nearly the entire southern ocean and anomalous cooling of the North Atlantic and the off-equatorial North Pacific is also associated with enhanced spatially integrated stationary ascent (Fig. 10a, b). We speculate that this association with interhemispheric SST contrast might be caused by ocean advection or by atmospheric advection: basic state currents or winds transport anomalous energy from one hemisphere preferentially into specific longitudes of the NH subtropics. For example, anomalously cold water in the high-latitude North Atlantic would be advected southward along the coast of Africa by the anticyclonic subtropical gyre, enhancing the zonal asymmetry in the subtropical Atlantic; northward Ekman flow in the Indian Ocean during boreal winter and spring could transport anomalously warm water from the southern ocean into the subtropical NH Indian Ocean. Alternatively, given a warm southern ocean and a cold high-latitude northern ocean, northward low-level monsoon winds would advect high-MSE air across the equator into the Indian Ocean, West

Africa, and the West Pacific, while the low-level anticyclones over the subtropical NH ocean would advect low-MSE air into the Sahara and East Pacific. Further work is necessary to elucidate which processes operate in models and in reality; here we suggest that models with an anomalously large increase in interhemispheric SST contrast have enhanced zonal gradients in subtropical NH MSE/SST, which in turn intensifies stationary ascent following (10). Though speculative, this would be consistent with SST changes causing stationary ascent changes; the converse would require changes in stationary ascent to produce warming of nearly the entire southern ocean.

4 Summary

Here we used a simple dynamical model, based on Sverdrup balance and the vertical structure of a first-baroclinic mode, to understand the response of subtropical stationary circulations to global warming. This model captures critical aspects of the sensitivity of stationary ascent to global warming as simulated in a large ensemble of comprehensive climate models: for instance, it represents the multi-model mean deepening and weakening of tropospheric stationary ascent seen in the model ensemble. Using this theoretical model, we tied changes in stationary ascent to changes in the tropopause level and to changes in zonal gradients of tropospheric temperature, then we associated those temperature gradient changes with changes in near-surface MSE and SST.

In particular, we showed that a modest weakening of stationary ascent in the CMIP5 ensemble-mean is in balance with a weakening of the zonal temperature gradient, which is partially opposed by the influence of the tropopause lifting. The weakening of zonal temperature gradients manifests partly as a change in the magnitude and partly as a change in the spatial pattern of zonal asymmetries in temperature, with both factors contributing nearly equally to the ensemble-mean change in temperature gradient. While spatial pattern changes are fairly robust across climate models, changes in the magnitude of tropospheric temperature anomalies are not consistent across models; the latter are associated with most of the intermodel scatter in stationary circulation strength changes with global warming.

Stationary ascent is tied to zonal temperature gradients through balance arguments that cannot determine causation, but we use convective quasi-equilibrium to associate the changes in tropospheric temperature gradients with changes in near-surface MSE and SST. This is especially significant in understanding intermodel variability, with intermodel variations in stationary ascent changes being associated with both zonal and meridional gradients in near-surface MSE and SST. The strong constraint of SST on near-surface MSE over oceans and the prevalence of ocean regions in the tropics suggests that zonal SST anomalies may play a significant role in driving changes in the strength of stationary circulations. In the CMIP5 ensemble-mean, zonal MSE gradients strengthen by about 4%/K; the ensemble-mean weakening of zonal

temperature gradients occurs because of the nonlinear dependence of saturation MSE on temperature (e.g. as the atmosphere warms, the upper-tropospheric temperature gradient would weaken if it were to maintain a constant gradient in upper-tropospheric saturation MSE).

Our results contrast with recent studies that highlighted the distinct roles of ocean warming and direct CO_2 forcing over land in controlling stationary circulation changes (e.g. Shaw and Voigt 2015), in that we find changes in subtropical stationary ascent are primarily associated with thermodynamic changes that cannot be partitioned simply between ocean and land. For example, models having the strongest amplification of subtropical stationary ascent over the next century also have an increase in the thermodynamic contrast between South Asia and North Africa, and between the Indian and Atlantic Oceans (Fig. 10a). If the effect of a globally uniform CO_2 increase were partitioned into its indirect effects that act via SST warming and its radiative forcing over land, we would expect the SST warming to reduce zonal gradients in free-tropospheric temperature during boreal summer (when upper-level temperature maxima are centered over land), weakening the stationary ascent and, as was shown by Shaw and Voigt (2015), weakening the stationary horizontal winds. Any tropopause lifting that accompanies the SST warming would oppose this weakening of stationary ascent, but the resulting net change in ascent would need to be assessed by a quantitative analysis of AMIP-style numerical model simulations that seems beyond the scope of this current work.

The effect of tropopause lifting on tropical circulations predicted by the mechanism presented here is apparently opposite to that predicted from the energetic mechanism of Chou and Chen (2010): that mechanism predicts that a lifting of the tropopause weakens tropical circulations by increasing the effective tropospheric static stability (i.e. the gross moist static stability). In the subtropics, however, variability in the gross moist stability need not constrain circulation changes because horizontal advection (ventilation) of MSE becomes significant (Chou et al. 2001; Chou and Neelin 2003). Here we find that tropopause lifting amplifies large-scale tropospheric ascent, as described by its effect on the first-baroclinic vertical wind mode (Fig. 8a, b). Using an entirely different argument, Singh and O'Gorman (2012) also argued that tropical circulations weaken following a lifting of the tropopause. In their transformation, horizontal winds are translated upward by global warming in a way that reduces the thickness of the upper troposphere and thus weakens integrated horizontal wind convergence and ascent strength. However, we find no evidence for a reduction in the depth of the upper tropospheric layer (when defined from the stationary vertical wind profile or that of its Sverdrup-baroclinic component, as in Figs. 4, 7). An assessment of the degree to which these various mechanisms operate in climate change scenarios is needed.

A better understanding of regional climate change requires improved theoretical models of tropical circulations. Here we use the stationary,

baroclinic Rossby gyre as the central element of a framework for understanding changes in stationary circulations with global warming, and devise quantitative scalings that account for a substantial fraction of these changes in a large ensemble of comprehensive climate models. We suggested that changes in zonal and interhemispheric SST gradients may be the underlying cause of changes in subtropical ascent, but further work is needed to more rigorously assess this causal relationship. Understanding how changes in stationary ascent are affected by ageostrophic winds, which were neglected in the simple framework used here, is another important task.

Table 1 List of reanalysis product and climate models used in this study

Index	Name	Institution	Horizontal resolution
A	ERA-INTERIM	European Centre for Medium-Range Weather Forecasts, UK	0.75° × 0.75°
1	ACCESS1-0	Commonwealth Scientific and Industrial Research Organisation, Australia	1.88° × 1.25°
2	ACCESS1-3	Commonwealth Scientific and Industrial Research Organisation, Australia	1.88° × 1.25°
3	BCC-CSM1-1	Beijing Climate Center, China	2.81° × 2.79°
4	BCC-CSM1-1-m	Beijing Climate Center, China	1.13° × 1.12°
5	BNU-ESM	Beijing Normal University, China	2.81° × 2.79°
6	CanESM2	Canadian Centre for Climate Modelling and Analysis, Canada	2.81° × 3.15°
7	CCSM4	National Center for Atmospheric Research, USA	1.25° × 0.94°
8	CESM1-BGC	National Center for Atmospheric Research, USA	1.25° × 0.94°
9	CESM1-CAM5	National Center for Atmospheric Research, USA	1.25° × 0.94°
10	CMCC-CESM	Euro-Mediterranean Center on Climate Change, Italy	3.75° × 4.17°
11	CMCC-CM	Euro-Mediterranean Center on Climate Change, Italy	0.75° × 0.84°
12	CMCC-CMS	Euro-Mediterranean Center on Climate Change, Italy	1.88° × 2.10°
13	CNRM-CM5	Centre National de Recherches Meteorologiques, France	1.41° × 1.58°
14	CSIRO-Mk3-6-0	Commonwealth Scientific and Industrial Research Organisation, Australia	1.88° × 2.10°
15	FGOALS-g2	Institute of Atmospheric Physics, China	2.81° × 4.89°
16	FIO-ESM	The First Institute of Oceanography, China	2.81° × 2.79°
17	GFDL-CM3	Geophysical Fluid Dynamics Laboratory, USA	2.50° × 2.00°
18	GFDL-ESM2G	Geophysical Fluid Dynamics Laboratory, USA	2.50° × 2.02°
19	GFDL-ESM2M	Geophysical Fluid Dynamics Laboratory, USA	2.50° × 2.02°
20	GISS-E2-H	NASA Goddard Institute for Space Studies, USA	2.50° × 2.00°
21	GISS-E2-H-CC	NASA Goddard Institute for Space Studies, USA	2.50° × 2.00°
22	GISS-E2-R	NASA Goddard Institute for Space Studies, USA	2.50° × 2.00°
23	GISS-E2-R-CC	NASA Goddard Institute for Space Studies, USA	2.50° × 2.00°
24	HadGEM2-AO	Met Office Hadley Centre, UK	1.88° × 1.25°
25	HadGEM2-CC	Met Office Hadley Centre, UK	1.88° × 1.25°
26	HadGEM2-ES	Met Office Hadley Centre, UK	1.88° × 1.25°
27	inmcm4	Institute for Numerical Mathematics, Russia	2.00° × 1.50°
28	IPSL-CM5A-LR	Institut Pierre-Simon Laplace, France	3.75° × 1.89°
29	IPSL-CM5A-MR	Institut Pierre-Simon Laplace, France	2.50° × 1.27°
30	IPSL-CM5B-LR	Institut Pierre-Simon Laplace, France	3.75° × 1.89°
31	MIROC5	Japan Agency for Marine-Earth Science and Technology, Japan	1.41° × 1.57°
32	MIROC-ESM-CHEM	Japan Agency for Marine-Earth Science and Technology, Japan	2.81° × 3.12°
33	MIROC-ESM	Japan Agency for Marine-Earth Science and Technology, Japan	2.81° × 3.12°
34	MPI-ESM-MR	Max Planck Institute for Meteorology, Germany	1.88° × 2.10°
35	MPI-ESM-LR	Max Planck Institute for Meteorology, Germany	1.88° × 2.10°
36	MRI-CGCM3	Meteorological Research Institute, Japan	1.13° × 1.26°
37	MRI-ESM1	Meteorological Research Institute, Japan	1.13° × 1.26°
38	NorESM1-ME	Norwegian Climate Center, Norway	2.50° × 1.89°
39	NorESM1-M	Norwegian Climate Center, Norway	2.50° × 1.89°

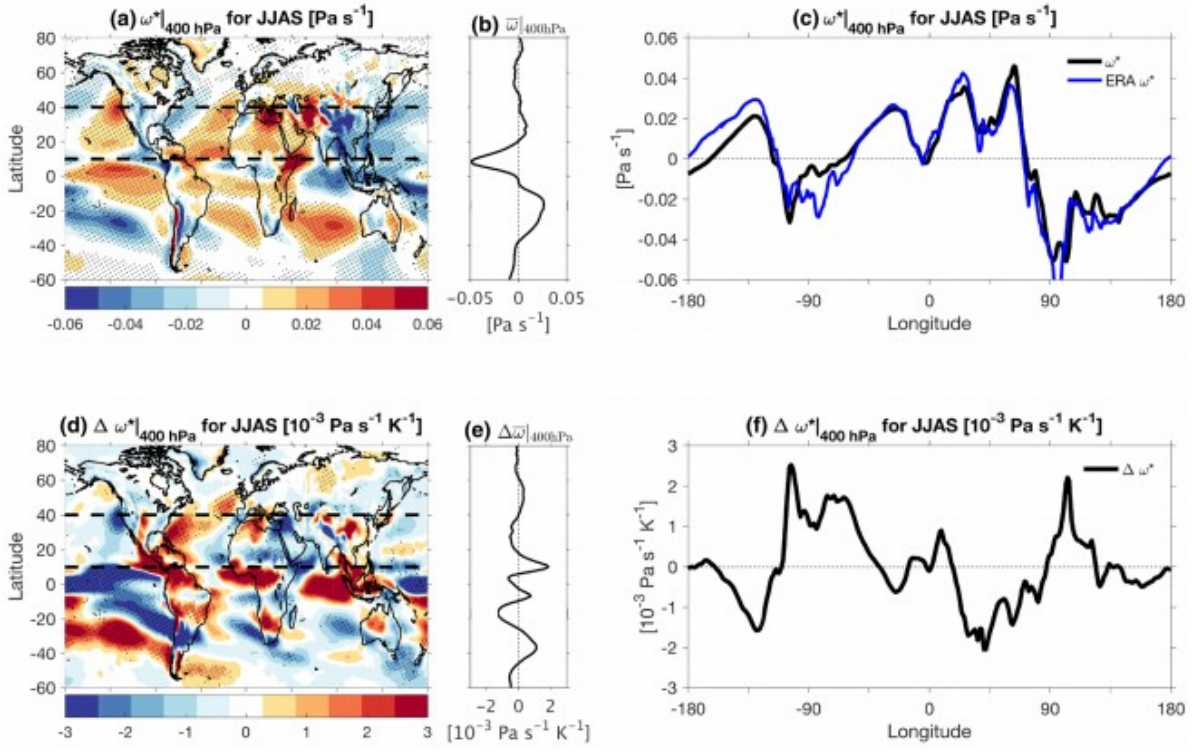

Fig. 1 Multi-model mean of boreal summer vertical wind for the historical simulations, evaluated at the 400 hPa isobar: **a** stationary vertical wind, **b** zonal-mean vertical wind, **c** longitudinal cross-section of stationary vertical wind averaged over the 10°N to 40°N latitudinal band, both for multi-model mean (black line) and reanalysis data (blue line, ERA-Interim). **d–f** Same as **a–c** but for changes between RCP8.5 and historical simulations; here, changes are normalized by the domain averaged surface temperature changes. Multi-model means are computed by averaging over all CMIP5 simulations listed on Table 1; boreal summer is defined from June to September; historical simulations and ERA-Interim output are averaged over the 1985–2004 period, and RCP8.5 output over the 2076–2095 period. Dashed black lines define bounds of the Northern Hemisphere subtropics set in this study (10°N to 40°N). Stippling shows regions where at least 80% of the models agree on the sign of the velocity

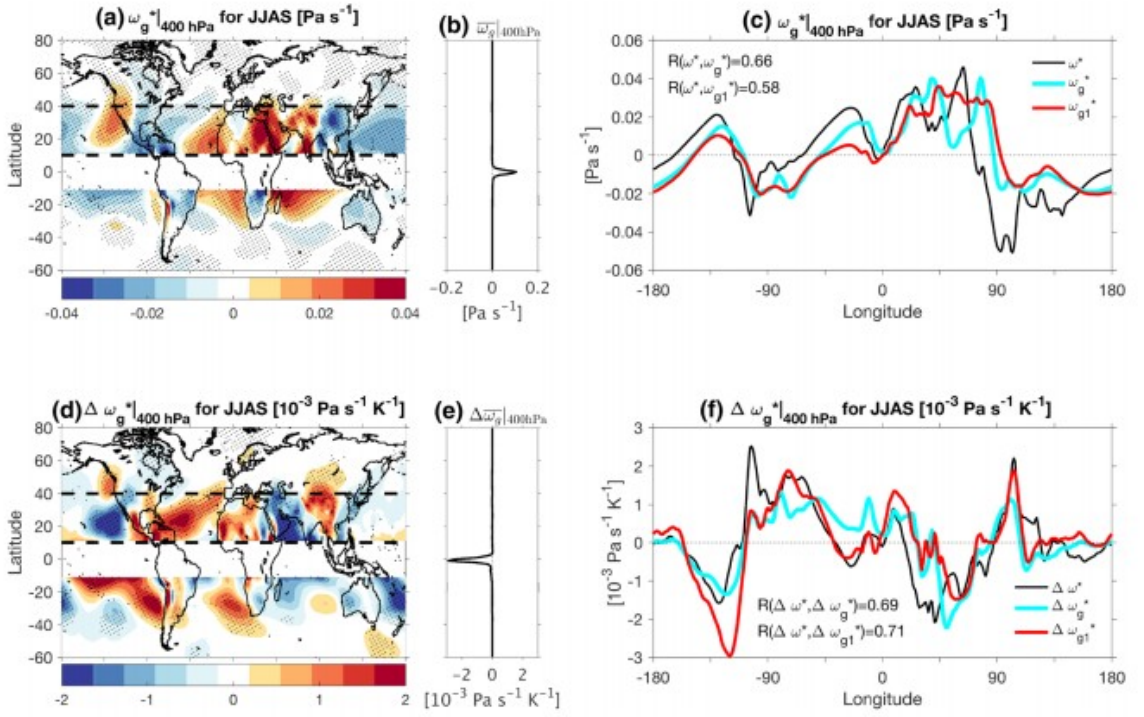

Fig. 2 Same as Fig. 1 but for the baroclinic, Sverdrup-balanced vertical wind (4), ω_g. Its first-baroclinic component, ω_{g1}, is also shown on **c** and **f** for comparison (red line). **b**, **e** The baroclinic, Sverdrup-balanced vertical wind in the zonal-mean, which nearly vanishes except near the equator where it is ill-defined (conservatively delimited within the 10°S and 10°N latitudinal band). On **a** and **d**, ω_g values have been masked where ill-defined

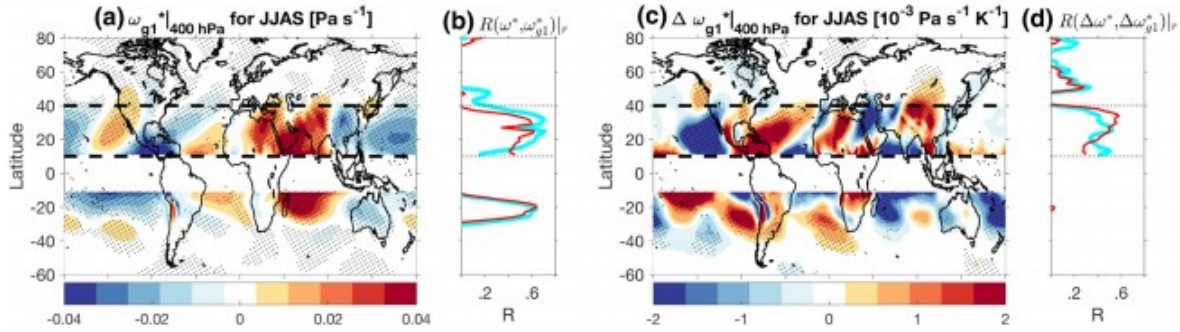

Fig. 3 Same as Fig. 1 but for the first-baroclinic, Sverdrup-balanced vertical wind (10): **a** its historical climatology, ω_{g1}, and **c** its changes with global warming, $\Delta\omega_{g1}$. The cyan [red] solid lines on side panels show the latitudinal profiles of the correlation coefficient for **b** ω^* on ω_g $[\omega_{g1}^*]$, and (d) $\Delta\omega^*$ on $\Delta\omega_g$ $*$ $[\Delta\omega_{g1}^*]$ (at 400 hPa)

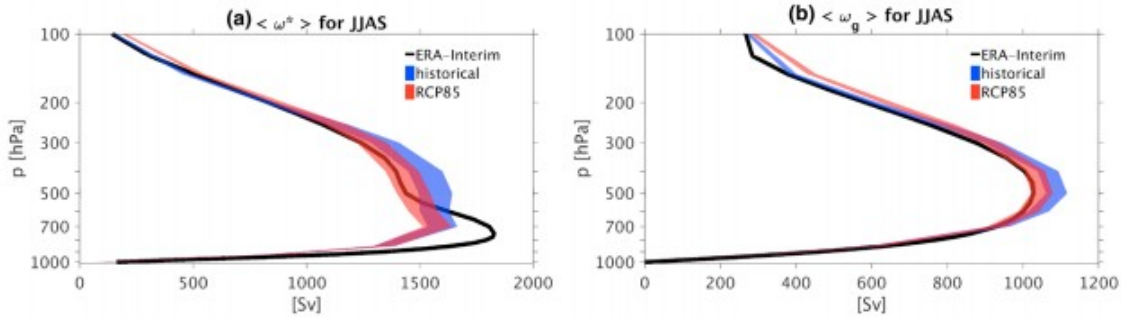

Fig. 4 **a** Stationary vertical wind profile integrated over the NH subtropics, $\langle \omega^* \rangle$, in the historical (blue band) and RCP8.5 simulations (red band). **b** Same as **a** but for the baroclinic, Sverdrup-balanced vertical wind, $\langle \omega_g \rangle$. Bands define the $\pm 2\sigma$ intermodel confidence interval in the plotted variables for historical (blue) and RCP8.5 simulations (red). Corresponding ERA-Interim reanalysis profiles are shown as well (black line)

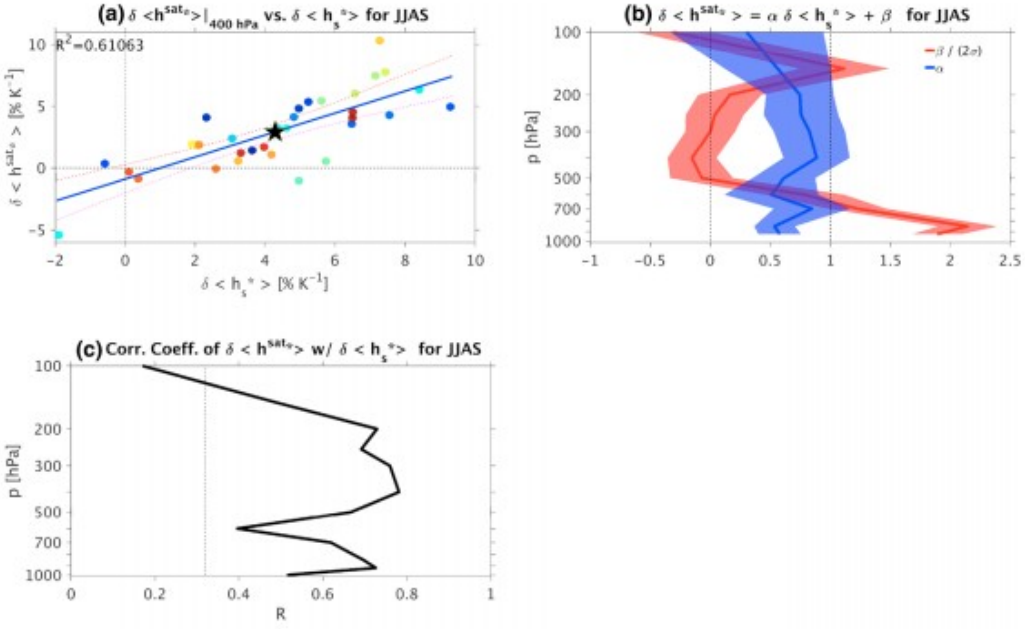

Fig. 5 **a** Saturation moist static energy (MSE) anomalies evaluated at the 400 hPa isobar vs. near-surface (2-m) MSE anomalies integrated over the NH subtropics [anomalies are normalized relative to near-surface temperature change averaged over the NH subtropics (%/K)]; each color dot on **a** refers to an individual GCM simulation, and blue line shows the best linear fit and dashed lines the 95% confidence interval for the regression line. **b** Intercept and slope profiles of regression line and **c** correlation coefficient profile between spatially integrated saturation MSE anomalies and spatially integrated near-surface MSE anomalies

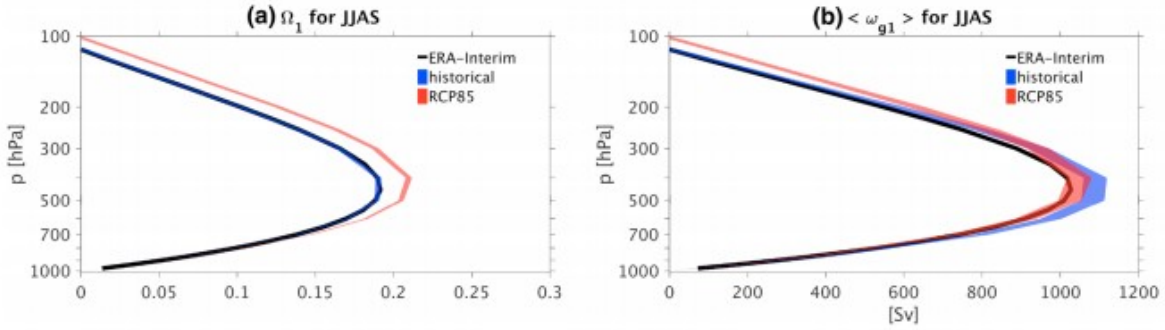

Fig. 6 Same as in Fig. 4 but for the **a** vertical wind mode profile, $\langle \Omega_1 \rangle$ and **b** first-baroclinic, Sverdrup-balanced vertical wind integrated over the NH subtropics, $\langle \omega_{g1} \rangle$

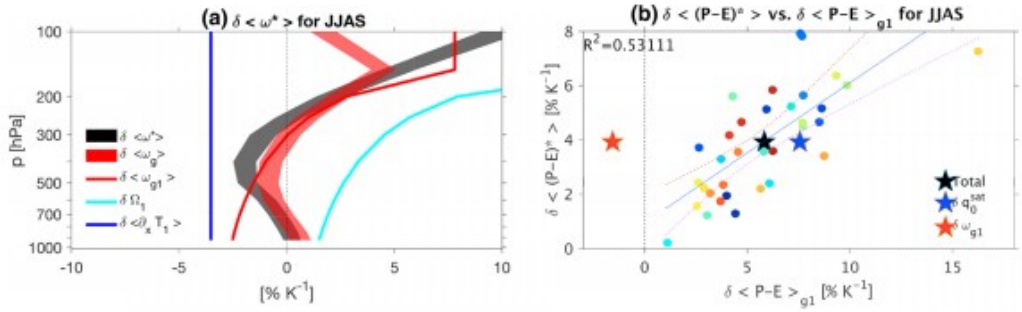

Fig. 7 **a** Changes in horizontally integrated stationary vertical wind (black band), baroclinic Sverdrup-balanced vertical wind (4) (red band), and its predicted first-baroclinic Sverdrup-balanced component (10) (red line); also shown are vertical wind mode (cyan line) and horizontally integrated temperature gradient (blue line) changes associated with changes in the Sverdrup-balanced, first-baroclinic vertical wind. **b** Change in horizontally integrated hydrologic imbalance anomalies $\langle (P-E)^* \rangle$ vs. its predicted value (11) when assuming it is driven by changes in the Sverdrup-balanced, first-baroclinic vertical wind as well as changes in saturation specific humidity profile q_0. The black star shows the ensemble-mean value of $\delta\langle (P-E)^* \rangle$ and $\delta\langle (P-E)_{g1} \rangle$; blue and red stars show thermodynamic and dynamic contributions to those changes. Plotting conventions as in Fig. 5

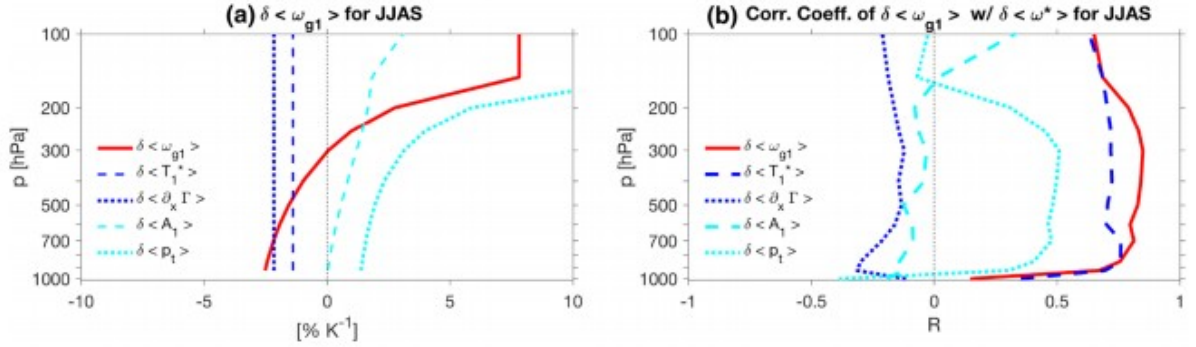

Fig. 8 **a** Change in the horizontally integrated Sverdrup-balanced, first-baroclinic vertical wind (10) and its contributions from changes in the amplitude of temperature anomalies (blue dashed line), horizontal structure of temperature anomalies (blue dotted line), tropopause level (cyan dotted line) and temperature mode (cyan dashed line). Sum of dashed and dotted blue (cyan) lines equals solid blue (cyan) line in Fig. 7a. **b** Intermodel correlation coefficient of the change in the horizontally integrated stationary vertical wind with variables shown in **a**. Same plotting convention in **a** and **b**

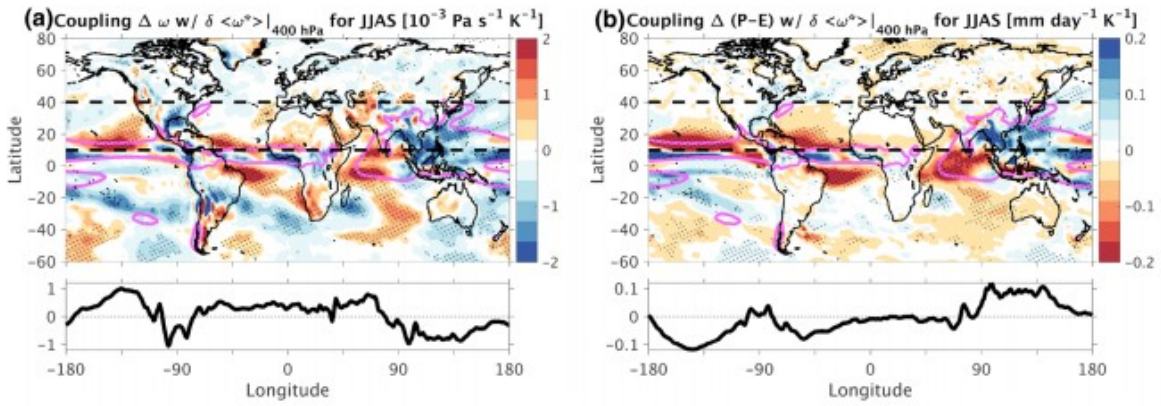

Fig. 9 Coupling of **a** vertical wind and **b** $P - E$ changes with changes in the horizontally integrated stationary ascent at 400 hPa. Longitudinal cross-sections show coupling indices averaged over NH subtropics. Magenta line shows the 5 mm/day precipitation isopleth; stippling on **a** and **b** indicates areas where coupling or slope is statistically significant at the 5% level

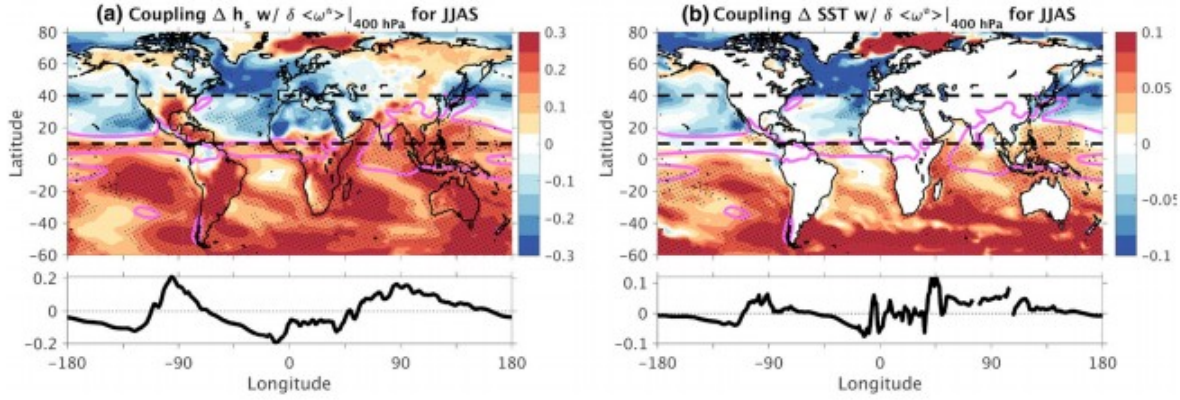

Fig. 10 Same as in Fig. 9 but for **a** near-surface MSE changes and **b** SST changes.

Acknowledgements

We are grateful to three anonymous reviewers for their insightful comments. Xavier J. Levine and William R. Boos were supported by National Science Foundation awards AGS-1515960 and AGS-1746160. CMIP5 output were obtained from the World Data Center for Climate (WDCC) website at https://cera-www.dkrz.de.

Appendix: Temperature mode definition

In this section, we provide an expression of the temperature mode in (7), which is used to define the vertical wind mode in (10). Its profile is central to our understanding of stationary ascent variability with climate change.

In Levine and Boos (2016) the temperature mode was defined as the sensitivity of tropospheric temperature to a temperature anomaly at the lifting condensation level (LCL). Here, we define the temperature mode as the magnitude of temperature anomalies associated with a unit temperature anomaly at any level above the LCL, i,e.

$$A_1(p) = \frac{1 + \gamma(p_r) + \beta(p_r)}{1 + \gamma(p) + \beta(p)} \quad \text{for} \quad p_t \le p \le p_b, \tag{14}$$

$$A_1(p) = \left(\frac{p}{p_b}\right)^{\kappa} \frac{1 + \gamma(p_r) + \beta(p_r)}{1 + \gamma(p_b) + \beta(p_b)} \quad \text{for} \quad p_b \le p \le p_s, \tag{15}$$

with,

$$\gamma = \partial_T q_0^{sat}, \tag{16}$$

$$\beta = \partial_T z_0. \tag{17}$$

Here $(.)_b$ denotes the LCL pressure, $(.)_r$ denotes the reference level, and ∂_T is a partial derivative with respect to temperature. This general definition of the temperature mode is identical to that derived in Levine and Boos (2016) when the reference level is the LCL. In this study, we define the LCL as the 925 hPa isobar, and the reference level is the 400 hPa isobar. The temperature mode (15) is substituted in the definition of horizontal and vertical wind modes, i.e.

$$\Omega_1 = \frac{1}{p_s} \int_{p_s}^{p} V_1 \, \mathrm{d}p, \tag{18}$$

where V_1 is the horizontal wind mode,

$$V_1 = A_1^+ - \frac{1}{p_t - p_s} \int_{p_s}^{p_t} A_1^+ \, \mathrm{d}p, \tag{19}$$

and A_1^+ is a wind basis derived from the momentum budget,

$$A_1^+ = \int_{p_s}^{p} \frac{A_1}{p} \, \mathrm{d}p. \tag{20}$$

A detailed derivation of the first-baroclinic wind modes can be found in Levine and Boos (2016), and this derivation is based on the earlier work on first-baroclinic mode dynamics (Yu et al. 1998; Neelin and Zeng 2000). The vertical wind mode in the ensemble-mean of the CMIP5 simulations and in the ERA-40 reanalysis are shown in Fig. 6a.

References

Bony S, Bellon G, Klocke D, Sherwood S, Fermepin S, Denvil S (2013) Robust direct effect of carbon dioxide on tropical circulation and regional precipitation. Nat Geosci 6:447–451

Brown RG, Bretherton CS (1995) A test of the strict quasi-equilibrium theory on long time and space scales. J Atmos Sci 72:624–638

Chen T-C (2010) Characteristics of summer stationary waves in the Northern Hemisphere. J Clim 23:4489–4507

Chen P, Hoerling MP, Dole RM (2001) The origin of the subtropical anticyclones. J Atmos Sci 58:1827–1835

Cherchi A, Alessandri A, Masina S, Navarra A (2011) Effects of increased CO_2 levels on monsoons. Clim Dyn 37:83–101

Cherchi A, Annamalai H, Masina S, Navarra A (2014) South Asian summer monsoon and the eastern Mediterranean climate: the monsoon-desert mechanism in CMIP5 simulations. J Clim 27:6877–6903

Chou C, Chen CA (2010) Depth of convection and the weakening of tropical circulation in global warming. J Clim 23:3019–3030

Chou C, Neelin JD (2003) Mechanisms limiting the northward extent of the Northern summer monsoons over North America, Asia, and Africa. J Clim 16:406–425

Chou C, Neelin JD (2004) Mechanisms of global warming impacts on regional tropical precipitation. J Clim 17:2688–2701

Chou C, Neelin JD, Su H (2001) Ocean–atmosphere–land feedbacks in an idealized monsoon. Q J R Meteorol Soc 127:1869–1891

Chou C, Neelin JD, Chen CA, Tu JY (2009) Evaluating the ‘rich-get-richer’ mechanism in tropical precipitation change under global warming. J Clim 22:1982–2005

Chou C, Wu T-C, Tan P-H (2013) Changes in gross moist stability in the tropics under global warming. Clim Dyn 41:2481–2496

Dai A, Li H, Sun Y, Hong L-C, Chou C, Zhou T (2013) The relative roles of upper and lower tropospheric thermal contrasts and tropical influences in driving Asian summer monsoons. J Geophys Res 118:7024–7045

Dee DP et al (2011) The ERA-Interim reanalysis: configuration and performance of the data assimilation system. Q J R Meteorol Soc 137:553–597

Emanuel KA (1995) On thermally direct circulations in moist atmospheres. J Atmos Sci 52:1529–1534

Gill AE (1980) Some simple solutions for heat-induced tropical circulation. Q J R Meteorol Soc 106:447–462

He J, Soden BJ (2017) A re-examination of the projected subtropical precipitation decline. Nat Clim Change 7:53–57

He J, Soden BJ, Kirtman B (2014) The robustness of the atmospheric circulation and precipitation response to future anthropogenic surface warming. Geophys Res Lett 41:2614–2622

He C, Wu B, Zou L, Zhou T (2017) Responses of the summertime subtropical anticyclones to global warming. J Clim 30:6465–6479

Held IM, Soden BJ (2000) Water vapor feedback and global warming. Annu Rev Energy Environ 25:441–475

Held IM, Soden BJ (2006) Robust responses of the hydrological cycle to global warming. J Clim 19:5686–5699

Kelly P, Kravitz B, Lu J, Leung LR (2018) Remote drying in the North Atlantic as a common response to precessional changes and CO_2 increase over land. Geophys Res Lett 45:3615–3624

Knutson TR, Manabe S (1995) Time-mean response over the tropical Pacific to increased CO_2 in a coupled ocean-atmosphere model. J Clim 8:2181–2199

Levine XJ, Boos WR (2016) A mechanism for the response of the zonally asymmetric subtropical hydrologic cycle to global warming. J Clim 29:7851–7867

Li X, Ting M (2017) Understanding the Asian summer monsoon response to greenhouse warming: the relative roles of direct radiative forcing and sea surface temperature change. Clim Dyn 49:2863–2880

Li W, Li L, Ting M, Liu Y (2012) Intensification of Northern Hemisphere subtropical highs in a warming climate. Nat Geosci 5:830–834

Li X, Ting M, Li C, Henderson N (2015) Mechanisms of Asian summer monsoon changes in response to anthropogenic forcing in CMIP5 models. J Clim 28:4107–4125

Liu Y, Wu G, Ren R (2004) Relationship between the subtropical anticyclone and diabatic heating. J Clim 17:682–698

Ma J, Xie SP (2013) Regional patterns of sea surface temperature change: a source of uncertainty in future projections of precipitation and atmospheric circulation. J Clim 26:2482–2501

Ma J, Yu JY (2014) Paradox in South Asian summer monsoon circulation change: lower tropospheric strengthening and upper tropospheric weakening. Geophys Res Lett 41:2934–2940

Ma J, Xie SP, Kosaka Y (2012) Mechanisms for tropical tropospheric circulation change in response to global warming. J Clim 25:2979–2994

Merlis TM, Schneider T (2011) Changes in zonal surface temperature gradients and Walker circulations in a wide range of climates. J Clim 24:4757–4768

Muller CJ, O'Gorman PA (2011) An energetic perspective on the regional response of precipitation to climate change. Nat Clim Change 1:266–271

Neelin JD (2007) The global circulation of the atmosphere, chapter 10. Moist dynamics of tropical convection zones in monsoons, teleconnections, and global warming. Princeton University Press, Princeton, pp 267–301

Neelin JD, Yu JY (1994) Modes of tropical variability under convective adjustment and the Madden–Julian oscillation. Part I: analytical theory. J Atmos Sci 51:1876–1894

Neelin JD, Zeng N (2000) A quasi-equilibrium tropical circulation model-formulation. J Atmos Sci 57:1741–1766

O'Gorman PA, Allan RP, Byrne MP, Previdi M (2012) Energetic constraints on precipitation under climate change. Surv Geophys 33:585–608

Reid GC, Gage KS (1981) On the annual variation in height of the tropical tropopause. J Atmos Sci 38:1928–1938

Rodwell MJ, Hoskins BJ (1996) Monsoons and the dynamics of deserts. Q J R Meteorol Soc 122:1385–1404

Rodwell MJ, Hoskins BJ (2001) Subtropical anticyclones and summer monsoons. J Clim 14:3192–3211

Scheff J, Frierson DMW (2012) Robust future precipitation declines in CMIP5 largely reflect the poleward expansion of model subtropical dry zones. Geophys Res Lett 39:L18704

Schneider T, O'Gorman PA, Levine XJ (2010) Water vapor and the dynamics of climate changes. Rev Geophys 48:RG3001

Seager R, Naik N, Vecchi GA (2010) Thermodynamic and dynamic mechanisms for large-scale changes in the hydrological cycle in response to global warming. J Clim 23:4651–4668

Seager R, Liu H, Henderson N, Simpson I, Kelley C, Shaw T, Kushnir Y, Ting M (2014a) Causes of increasing aridification of the Mediterranean region in response to rising greenhouse gases. J Clim 27:4655–4676

Seager R, Neelin D, Simpson I, Isla H, Liu N, Henderson T, Shaw Y, Ting Kushnir M, Cook B (2014b) Dynamical and thermodynamical causes of large-scale changes in the hydrological cycle over North America in response to global warming. J Clim 27:7921–7948

Shaw TA, Voigt A (2015) Tug of war on summertime circulation between radiative forcing and sea surface warming. Nat Geosci 8:560–566

Shaw TA, Voigt A (2016a) Land dominates the regional response to CO_2 direct radiative forcing. Geophys Res Lett 43:11383–11391

Shaw TA, Voigt A (2016b) Understanding the links between subtropical and extratropical circulation responses to climate change using aquaplanet model simulations. J Clim 29:6637–6657

Singh MS, O'Gorman PA (2012) Upward shift of the atmospheric general circulation under global warming: theory and simulations. J Clim 25:8259–8276

Sun Y, Ding Y (2011) Responses of South and East Asian summer monsoons to different land-sea temperature increases under a warming scenario. Chin Sci Bull 56:2718–2726

Sun Y, Ding Y, Dai A (2010) Changing links between South Asian summer monsoon circulation and tropospheric land-sea thermal contrasts under a warming scenario. Geophys Res Lett 37:L02704

Tanaka HL, Ishizaki N, Kitoh A (2004) Trend and interannual variability of Walker, monsoon and Hadley circulations defined by velocity potential in the upper troposphere. Tellus A 56:250–269

Taylor KE, Stouffer RJ, Meehl GA (2012) An overview of CMIP5 and the experiment design. Bull Am Meteorol Soc 93:485–498

Ting M (1994) Maintenance of northern summer stationary waves in a GCM. J Atmos Sci 51:3286–3308

Tokinaga H, Xie SP, Deser C, Kosaka Y, Okumura YM (2012) Slowdown of the Walker circulation driven by tropical Indo-Pacific warming. Nature 491:439–443

Trenberth KE, Stepaniak DP, Caron JM (2000) The global monsoon as seen through the divergent atmospheric circulation. J Clim 13:3969–3993

Tyrlis E, Lelieveld J, Steil B (2013) The summer circulation over the eastern Mediterranean and the Middle East: influence of the South Asian monsoon. Clim Dyn 40:1103–1123

Ueda H, Iwai A, Kuwako K, Hori ME (2006) Impact of anthropogenic forcing on the Asian summer monsoon as simulated by eight GCMs. Geophys Res Lett 33:L06703

Vecchi GA, Soden BJ (2007) Global warming and the weakening of the tropical circulation. J Clim 20:4316–4340

Wang H, Ting M (1999) Seasonal cycle of the climatological stationary waves in the NCEP-NCAR reanalysis. J Atmos Sci 56:3892–3919

Webster PJ (1972) Response of the tropical atmosphere to local, steady forcing. Mon Weather Rev 100:518–541

Wills RC, Schneider T (2015) Stationary eddies and the zonal asymmetry of net precipitation and ocean freshwater forcing. J Clim 28:5115–5133

Wills RC, Levine XJ, Schneider T (2017) Local energetic constraints on Walker circulation strength. J Atmos Sci 74:1907–1922

Xie SP, Deser C, Vecchi GA, Ma J, Teng H, Wittenberg AT (2010) Global warming pattern formation: sea surface temperature and rainfall. J Clim 23:966–986

Yang F, Kumar A, Schlesinger ME, Wang W (2003) Intensity of hydrological cycles in warmer climates. J Clim 16:2419–2423

Yu J-Y, Chou C, Neelin JD (1998) Estimating the gross moist stability of the tropical atmosphere. J Atmos Sci 55:1354–1372

Zhou T, Yu R, Zhang J, Drange H, Cassou C, Deser C, Hodson DLR, Sanchez-Gomez E, Li J, Keenlyside N, Xin X et al (2009) Why the western Pacific subtropical high has extended westward since the late 1970s. J Clim 22:2199–2215